Three-Dimensional Simulations of Cavity Flows by the Space-Time CESE Method

Hao He,[*] S.-T. John Yu,[†] and Moujin Zhang[‡]
The Ohio State University, Columbus, Ohio, 43202

In this paper we report three-dimensional numerical simulation of compressible flows over open cavities. For high-fidelity unsteady solutions, we employ the Space-Time Conservation Element and Solution Element (CESE) method, a novel numerical method based on a unified treatment of space and time in calculating flux balance. High-speed cavity flows are studied to understand the mechanisms of mixing enhancement and flame holding by cavities. Numerical results are compared with the experimental data for dominant frequencies and time-averaged pressure coefficients inside the cavities. Numerical results show that cavity flows are highly three-dimensional and requires fine resolution of the shear layer over the open cavity. While the frequency of the pressure fluctuations can be easily captured, further mesh refinement and better control of numerical damping will be needed to improve the prediction of the pressure coefficient profiles inside the cavity.

I. Introduction

FUEL injection, ignition, and flame-holding are challenging issues for high-speed combustion. In a scramjet engine, the fuel injection method employed must provide rapid fuel/air mixing with minimum total-pressure loss in the air stream. A stable flame-holding system under a wide range of operating conditions is critical to sustain the supersonic combustion. Recently, cavity-based flame holders, an integrated mixing-enhancement and flame-holding approach, have attracted considerable attention in the scramjet community. Under suitable conditions, flow recirculation, or the trapped vortices, significantly increases the flow residence time of the fluid entering the cavity. A pilot flame could be set up inside the cavity to provide a pool of hot chemical radicals, which in turn would reduce the ignition delay of the air/fuel mixture in air stream and thus sustain high-speed combustion.

High-speed cavity flows are inherently unsteady, involving both broadband small scale fluctuations typical of turbulent flows, as well as distinct resonance with harmonic properties in its frequencies and amplitudes. In the past, it has been demonstrated that the aspect ratio of the cavity and free stream flow conditions are the critical parameters dominating the complex flow features, including boundary layer separation, compressible free shear layer with shedding vortices, linear/nonlinear acoustic waves, and complex shock and expansion waves interacting with vortices and acoustic waves.

In the setting of wheel wells and bomb bays, previous studies for high-speed cavity flows showed that cavity flows could be categorized into the following two groups: (i) open cavity flows, when $L/D < 7\sim10$, and (ii) closed cavity flows, when $L/D > 7\sim10$, where L denotes the length of the cavity, and D the depth. In flows over cavities of large aspect ratios ($L/D > 7\sim10$), the separated free shear layer emanating from the upstream corner of the cavity reattaches to the bottom wall of the cavity and results in two separated recirculation zones near the two corners between the lateral walls and the cavity floor. The resultant low pressure zones at the lower corners and high pressures on the cavity floor, where the shear layer reattaches, lead to significant drag and pressure loss of the air stream. In this case, mass addition/ejection into/from the cavity by aerodynamic unsteadiness is low to moderate, and the flow is referred to as "closed."

[*] Ph. D., Mechanical Engineering Department, and AIAA Student Member.
[†] Associate Professor, Mechanical Engineering Department, and AIAA Member.
[‡] Research Associate, Mechanical Engineering Department, and AIAA Member.

On the other hand, flows over cavities with smaller aspect ratios, L/D < 7~10, result in reattachment of the free shear layer to the rear bulkhead of the cavity. The impingement of the free shear layer on the rear lateral wall causes violent unsteady motions and results in significant periodical mass addition/ejection near the rear bulkhead of the cavity, and the flows are referred to as "open." The wave patterns of open cavity flows could be further categorized into (i) transverse mode for very short cavities, L/D ≅ 1, and (ii) longitudinal mode for longer cavities, e.g., 2~3 < L/D < 7~10. In short cavities, L/D < 2, only one main vortex inside the cavity is sustained by the driving shear layer spanning the top of the cavity. The up and down motions of the single main recirculation bubble generate acoustic waves, which by and large propagate in the direction perpendicular to the free shear layer, provided the free stream is transonic. The propagating waves are referred to as in a transverse mode. On the other hand, when the cavity is longer, 2~3 < L/D < 7~10, multiple moving vortices occur inside the cavity leading to complex interactions among trapped vortices, propagating and rebounding pressure waves, and the flapping free shear layer. In general, the rebounding pressure waves, while interacting with the free shear layer, drastically amplify the growth rate of the free shear layer, which in turn sheds enormous vortices propagating towards and impinging on the aft wall of the cavity. Due to propagating vortices in the stream wise direction and the rebounding pressure waves, prevalent acoustic waves propagate in the longitudinal direction outside the cavity into the downstream area. If the air stream is transonic or subsonic, the acoustics would transversely propagate into the upstream areas.

In the setting of supersonic combustion inside a scramjet engine, trapped vortices inside cavities could be useful for flame holding. Moreover, cavity resonance, which produces periodic mass addition/expulsion with large flow structures, could be useful for mixing enhancement. Simultaneously, cavity drag must be minimum, e.g., much less than that of a bluff body, and thus only causes acceptable pressure loss. Gruber et al. [1, 2] have developed a dual-mode ramjet/scramjet engine concept, which is envisioned to use hydrocarbon fuels for a flight regime of Mach numbers from 3 to 6 ~ 9. In their supersonic combustors [1, 2], open cavities with aspect ratios about 5 < L/D < 8 have been tested in conjunction with various fuel injection schemes. Numerical simulation of cavity flows has been conducted by Baurle et al. [3]. The results showed that the cavities have great potential to be a viable combined flameholder/mixing enhancement device for scramjet engine combustor. Similar ideas have also been independently proposed and tested by Yu et al. [4]. In particular, Yu et al. [4] has tested supersonic flows passing multiple cavities. Some of recent results have been summarized by Ben-Yaker and Hanson [5].

In the past, extensive experimental and theoretical studies on cavity flows have been conducted for applications in wheel well and bomb bay, and flow characteristics such as the oscillation frequency and amplitudes at various locations in the cavity have been reported [6-11]. However, it is difficult to directly apply this knowledge base to cavity flows for the advanced scramjet engines due to much shorter length/time scales in scramjet engine. Additional complexity associated with fuel injection also warrants further studies because cavity flows and the associated acoustics would be drastically changed by the fuel injection schemes employed. In particular, inherent oscillations of cavity flows may be significantly suppressed by an upstream injection [4, 9-11].

In the present paper, we focus on time-accurate calculation of high-speed cavity flows. The objectives of the present study are: (i) to validate the numerical results by assessing the calculated frequencies and amplitudes of pressure oscillations and compared them with previous reported data, and (ii) to demonstrate the capabilities of the CESE method for capturing complex flow features of the supersonic cavity flows. The rest of this extended abstract is organized as follows. Section 2 reviews the model equations to be solved by the CESE method. Section 3 provides background information of the CESE method. Section 4 shows preliminary numerical solutions. We then offer concluding remarks and provide cited references.

II. The Model Equations

Equation (2.1) shows the vector form of the three-dimensional flow equations in Cartesian coordinates, including the continuity equation, the Navier-Stokes equations, the energy equation, and one species equation:

$$\frac{\partial \mathbf{U}}{\partial t}+\frac{\partial \mathbf{F}}{\partial x}+\frac{\partial \mathbf{G}}{\partial y}+\frac{\partial \mathbf{H}}{\partial z}-\frac{\partial \mathbf{F}_V}{\partial x}-\frac{\partial \mathbf{G}_V}{\partial y}-\frac{\partial \mathbf{H}_V}{\partial z}=0 \tag{2.1}$$

where the flow variable vector

$$\mathbf{U}=\left(\rho,\rho u,\rho v,\rho e,\rho w,\rho Y_f\right)^T, \tag{2.2}$$

the inviscid flux vectors are

$$\mathbf{F}=\begin{pmatrix}\rho u\\ \rho u^2+p\\ \rho uv\\ \rho uw\\ u(\rho e+p)\\ \rho uY_f\end{pmatrix},\quad \mathbf{G}=\begin{pmatrix}\rho v\\ \rho uv\\ \rho v^2+p\\ \rho vw\\ v(\rho e+p)\\ \rho vY_f\end{pmatrix},\quad \mathbf{H}=\begin{pmatrix}\rho w\\ \rho uw\\ \rho vw\\ \rho w^2+p\\ w(\rho e+p)\\ \rho wY_f\end{pmatrix} \tag{2.3}$$

and the viscous flux vectors are

$$\mathbf{F}_v=\begin{pmatrix}0\\ \tau_{xx}\\ \tau_{xy}\\ \tau_{xz}\\ u\tau_{xx}+v\tau_{xy}+w\tau_{xz}-q_x\\ -\rho\hat{u}_fY_f\end{pmatrix},\mathbf{G}_v=\begin{pmatrix}0\\ \tau_{xy}\\ \tau_{yy}\\ \tau_{zy}\\ u\tau_{xy}+v\tau_{yy}+w\tau_{zy}-q_y\\ -\rho\hat{v}_fY_f\end{pmatrix},\mathbf{H}_v=\begin{pmatrix}0\\ \tau_{xz}\\ \tau_{yz}\\ \tau_{zz}\\ u\tau_{xz}+v\tau_{yz}+w\tau_{zz}-q_z\\ -\rho\hat{w}_fY_f\end{pmatrix} \tag{2.4}$$

In the above equations, ρ is the density; u, v, and w are velocity components in the x, the y, and the z directions, respectively; p is the static pressure; $e = \varepsilon + \frac{1}{2}(u^2 + v^2+w^2)$ is the specific total energy with ε as the specific internal energy. We assume the fluid is ideal and polytropic. Due to the equation of state of an ideal gas, $p = (\gamma - 1)\rho\,\varepsilon$, where $\gamma = C_p/C_v$ is the specific heat ratio and it is a constant. In the viscous vectors, τ_{xx}, τ_{xy}, τ_{yy}, τ_{xz}, τ_{zy}, and τ_{zz} are stress components, and q_x, q_y, and q_z are the heat conduction fluxes in the x, the y, and the z directions, respectively. Y_f is the mass fraction of fuel. The diffusion velocity components, $\hat{u}$, $\hat{v}$ and $\hat{w}$ are calculated by Fick's law, e.g.,

$$Y_f\hat{u}_f=-D\frac{\partial Y_f}{\partial x} \tag{2.5}$$

where *D* is the mass diffusivity of fuel in the gas mixture. Diffusion fluxes in the y and z directions are defined in a similar way. The molecular viscosity μ is calculated using Sutherland's law [12] and the Lewis number Le =1 is assumed to calculate the mass diffusivity D. In numerical calculations, the above governing equations are nondimensionalized by the free stream conditions, i.e., velocity components by u_∞, density by ρ_∞, pressure by $\rho_\infty u_\infty^2$, and the total energy by $\rho_\infty u_\infty^2$. The subscript ∞ denotes the free stream condition. The cavity depth d is used as the length scale, and the time scale is d/u_∞.

III. The CESE Method

In order to faithfully track all linear and nonlinear waves, the numerical method employed must be able to capture all interactions between time marching terms and nonlinear flux terms, which give rise to the generalized Riemann problem involving multiple waves propagating at different speeds according to the eigenvalues of the coefficient matrixes of the Euler equations. The CESE method is a novel numerical framework for high-fidelity solution of hyperbolic conservation laws. Originally developed by Chang and coworkers [13-18], the tenet of the CESE method is a unified treatment of space and time in calculating flux balance. Contrast to modern upwind schemes, no Riemann solver and/or a reconstruction procedure is used as the building block of the CESE method. As a result, the logic and computational counts of the CESE method are simpler and more efficient. Based on the CESE method, computer programs for solving unsteady flows in one, two, and three spatial dimensions for structured, and unstructured meshes, and for meshes composed of mixed elements have been developed. These solvers have been parallelized based on domain decomposition in conjunction of the use of MPI. Previously, various flow phenomena have been calculated by using the CESE method. In particular, the CESE solver is capable of calculating high-speed compressible flow as well as flows at very low Mach numbers without applying preconditioning to the governing equations. Moreover, the CESE method is capable of simultaneously capture strong shock waves and the acoustic waves in the same computational domain, while the amplitude of the pressure jump across the shock wave would be several orders of magnitude higher than that of the acoustic waves.

The CESE method employed in the present paper is based on the use of hexagonal cells in the three-dimensional space [17], which was extended from the original CESE method. For conciseness, we will only illustrate the basic ideas of the CESE method in the present paper. To proceed, we consider the NS equations, Eq. (2.1), for gas dynamics and let $x_1 = x$, $x_2 = y$, $x_3 = z$ and $x_4 = t$ as the coordinates of a four-dimensional space-time Euclidean space E_4. By using the divergence theorem, the Euler equations become

$$\oint_{S(V)} \mathbf{h}_m \cdot d\mathbf{s} = 0\,, \qquad m=1,2,\ldots,6 \tag{3.1}$$

where $S(V)$ is the surface of an space-time region V in E_4, $d\mathbf{s}$ is a surface element vector pointing outward, and $\mathbf{h}_m$ is the space-time current density vector. Equation (3.1) states that the total space-time flux $\mathbf{h}_m$ leaving volume V through $S(V)$ must conserve. The CESE method integrates Eq. (3.1) in E_4 and solves for the flow variables $\mathbf{U}$ at each new time level.

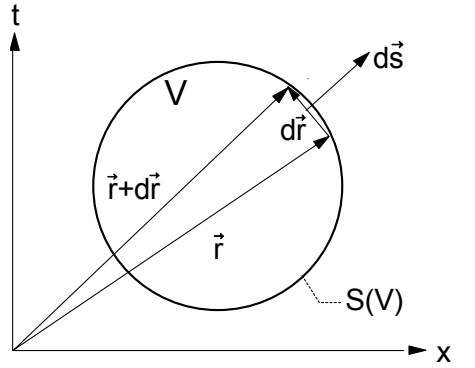

Fig 3.1: A schematic of space-time integral of the CESE method.

To integrate Eq. (3.1), the CESE method employs separate definitions of conservation element (CE) and solution element (SE). CEs are non-overlapping domains such that flux conservation is enforced over each CE, or over a union of neighboring CEs. Inside each CE, flow discontinuity is allowed. SEs are non-overlapping space-time domains such that within a SE flow variable and fluxes are assumed continuous and they are approximated by the first-order Taylor series expansion. We note that flow variables and fluxes could be discontinuous across neighboring SEs. In general, SEs do not coincide with CEs.

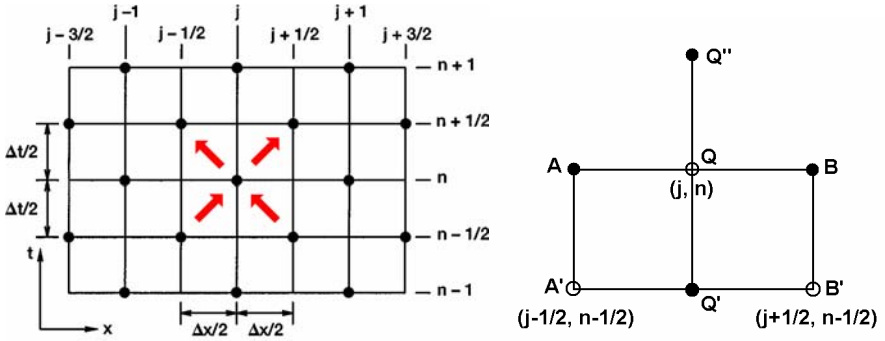

(a) (b)

Fig. 3.2: Schematics of the one-dimension CESE method. (a) The space-time mesh and (b) SE (j, n) and CE (j, n).

For conciseness, the discussion of the numerical solution of Eq. (3.1) will be restricted to one spatial dimension. Figure 3.1 shows space-time flux conservation by Eq. (3.1). To integrate Eq. (3.1) over a space-time domain, i.e., $S(V)$ in Fig. 3.1, we discretize the space-time domain as shown in Fig. 3.2, in which time marching of the CESE method is based on a space-time staggered mesh such that the flow information propagates only in one direction across the interfaces of neighboring CE and towards the future without encountering a Riemann problem. Figure 3.2(b) shows the CE and the SE associated with grid node (j, n). The SE is composed of two line segments: Q'Q" and AB, and their immediate neighborhood. The CE is the rectangle ABB'A'. For any (x, t) within SE(j, n), $u_m(x, t)$ and $f_m(x, t)$ are discretized based on the first-order Taylor expansion, denoted by the superscript *:

$$u_m^*(x,t;j,n) = (u_m)_j^n + (u_{mx})_j^n (x - x_j) + (u_{mt})_j^n (t - t^n)\,, \tag{3.2}$$

$$f_m^*(x,t;j,n) = (f_m)_j^n + (f_{mx})_j^n (x - x_j) + (f_{mt})_j^n (t - t^n)\,. \tag{3.3}$$

$$\mathbf{h}_m^*(x,t;j,n) = (f_m^*(x,t,j,n), u_m^*(x,t,j,n))\,. \tag{3.4}$$

Equation (3.1) is then approximated by the discrete form:

$$\oint_{S(CE)} \mathbf{h}_m^* \cdot d\mathbf{s} = 0 \cdot \tag{3.5}$$

Without providing the details, we substitute Eqs. (3.2-4) into Eq. (3.5) and get

$$(u_m)_j^n = \left[(u_m)_{j-1/2}^{n-1/2} + (u_m)_{j+1/2}^{n-1/2} + (r_m)_{j-1/2}^{n-1/2} - (r_m)_{j+1/2}^{n-1/2} \right] / 2 , \tag{3.6}$$

where

$$(r_m)_j^n = (\Delta x / 4)(u_{mx})_j^n + (\Delta t / \Delta x)(f_m)_j^n + (\Delta t^2 / 4\Delta x)(f_{mt})_j^n . \tag{3.7}$$

Equations (3.6-7) are the algorithm for solving u_m.

In two spatial dimensions, the computational domain is divided into non-overlapping quadrilaterals. Refer to Fig. 3.3(a). Vertices and centroids of quadrilaterals are marked by dots and circles, respectively. Q is the centroid of the quadrilateral $B_1B_2B_3B_4$. Points A_1, A_2, A_3, and A_4, respectively, are the centroids of the four neighboring quadrilaterals of the quadrilateral $B_1B_2B_3B_4$. Q^* marked by a cross in Fig. 3.3(a), is the centroid of the polygon $A_1B_1A_2B_2$ $A_3B_3A_4B_4$. Point Q^*, which generally does not coincide with point Q, is referred to as the solution point associated with Q. Note that points $A_1^*, A_2^*, A_3^*,$ and A_4^*, which are also marked by crosses, are the solution points associated with the centroids A_1, A_2, A_3, and A_4, respectively. To proceed, we consider the space-time mesh shown Fig. 2.3(b). Here $t = n\Delta t$ at the nth time level, where n = 0, 1/2, 1, 3/2, … For a given n, Q, Q', and Q'', respectively, denote the points on the n^{th}, the $(n\text{-}1/2)^{\text{th}}$, and $(n\text{+}1/2)^{\text{th}}$ time levels with point Q being their common spatial location. Other space-time mesh points in Fig. 3.3(b) are defined similarly. Without going into details of the algorithm, Fig. 3.3(c) represents a three-dimensional spatial mesh of the CESE method for flow in a three-dimensional space.

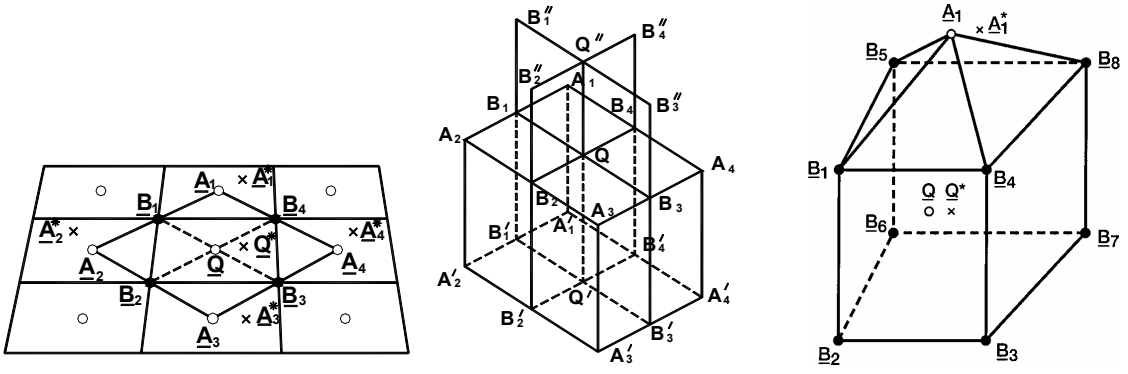

(a) (b) (c)

Fig. 3.3: The space-time mesh in multi spatial dimensions: (a) 2D grid points in the x-y plane, (b) SE and CE for the 2D scheme, (c) 3D grid points in the x-y-z space.

For unsteady flow calculations, numerical treatment to achieve non-reflecting boundary condition is a critical issue. In the setting of the CESE method, we are concerned with the integral equation and the conventional ideas of treating non-reflective boundary based on differential equations, e.g., the MOC asymptotic and matching analytical at far field, are inapplicable. Here, the non-reflecting boundary condition treatment is based on flux conservation near the computational boundary and letting the flux from the interior domain to smoothly exit to the computational domain through flux balance over boundary CEs. Because each CE allows flux and the flow information to propagate into the future, implementation of this flux-based boundary condition is extremely simple.

IV. Results and Discussions

Three cavity flows were considered: (i) a supersonic cavity flow taken from the supersonic combustion facility and the testing condition in the US AFRL supersonic combustion facility reported by Gruber et al. [1, 2] and Baurle et al. [5], (ii) a supersonic cavity taken from the experiments conducted by Stalling and Wilcox [20] in NASA Langley, and (iii) a subsonic cavity taken from the experiments conducted by Tracy and Plentovich [21] also in NASA Langley. Obviously, the most important issue of the LES 3D simulations is the numerical accuracy of the simulated results. Table 1 outline of the 3 cases studies in the present paper.

Table 1: Three high-speed cavity flows simulated by the CESE method.

Case	Free-Stream Mach number	Cavity Geometry	Mesh size	Accuracy validation	Reference
1	2	L/D = 7.76, W/D = 3.9	4 M	None	Gruber et al. [1,2] Baurle et al. [5]
2	2.86	L/D =12 , W/D =5	4.6 M	Averaged Cp profiles	Stalling and Wilcox [20]
3	0.95	L/D = , W/D =		Dominant frequencies	Tracy and Plentovich [21]

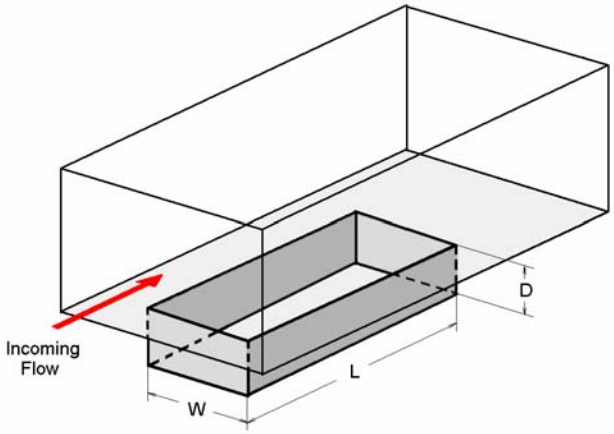

Fig. 4.1: The overall flow geometry and the computational domain.

Case 1: Mach 2 Cavity Flow

The flow condition and cavity geometry are taken from the supersonic combustion facility and the testing condition in the US AFRL supersonic combustion facility reported by Gruber et al. [1, 2] and Baurle et al. [5]. A supersonic flow at Mach 2 and Reynolds number of $4x10^5$ passes a swallow cavity with L/D = 7.76, where L and d are the length and depth of the cavity, respectively. The computational domain outside of the cavity is $0 \le x \le 11.52$, and $0 \le y \le 3.82$, where x and y are non-dimensionalized by D. Mesh points were clustered at the forward and aft bulkheads, at the plane spanning over the cavity mouth, and along the lateral sidewalls of the cavity.

About 4 million hexagonal elements are used for the computational domain. Figure 4.2 shows the mesh. The non-reflecting boundary condition is applied to the free stream surfaces, the de surfaces and the outlet surface. Initially, velocities inside the cavity are set to zero, and the density and pressure of the whole domain are set to the free stream values. The time step was chosen such that CFL ≈ 0.8 based on the free stream condition. Figure 4.2 also shows the domain decomposition for parallel computation. Difference colors represent difference sub-domains calculated by different CPU nodes. The domain decomposition is performed based on even distribution of the CPU work load and minimum communication among the nodes.

Figures 4.3 shows the iso-surfaces of constant pressure and the magnitude of vorticity. In this case, the cavity flow is far removed from being a two-dimensional flow. In particular, two vortex tubes along the side edges of the cavity could be clearly seen in Fig. 4.3(b). Figures 5 and 6 show snapshots of pressure contours and vorticity contours on the central plane of the cavity. Figure 4.4 shows the snapshots of streamwise component of the vorticity vector on a cross section plane of x = 6D from the leading edge of the cavity. Again, tremendous secondary recirculation can be clearly seen and the flow is high three-dimensional and unsteady.

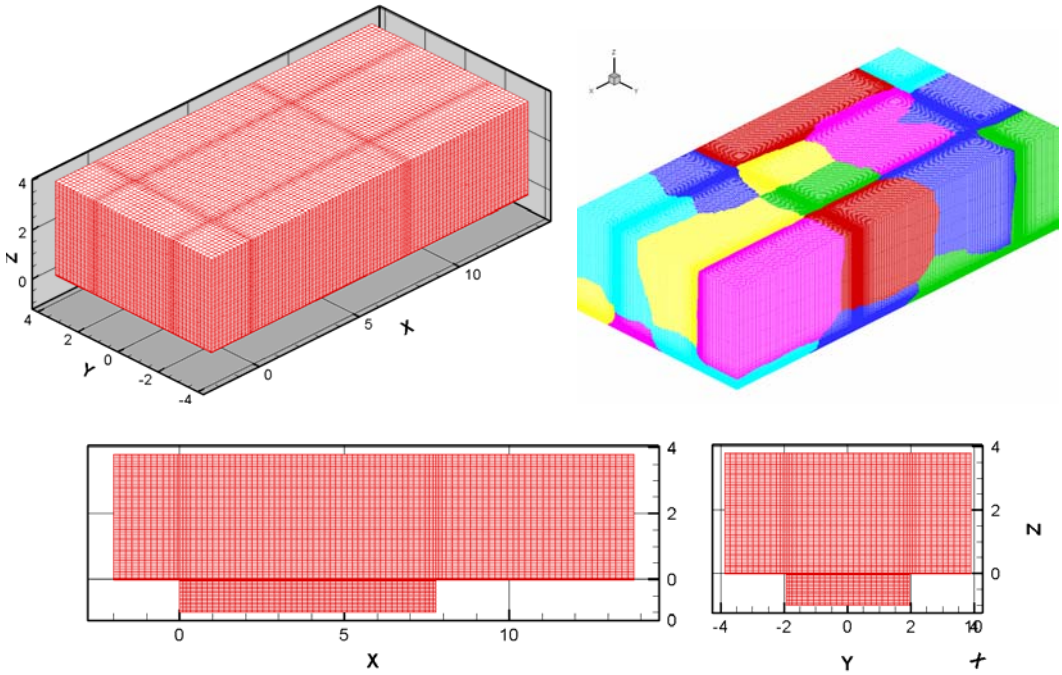

Fig. 4.2: Three-dimensional hexagonal mesh of Case (i). Domain decomposition by using METIS. Different colors represent different sub-domains calculated by different CPU nodes.

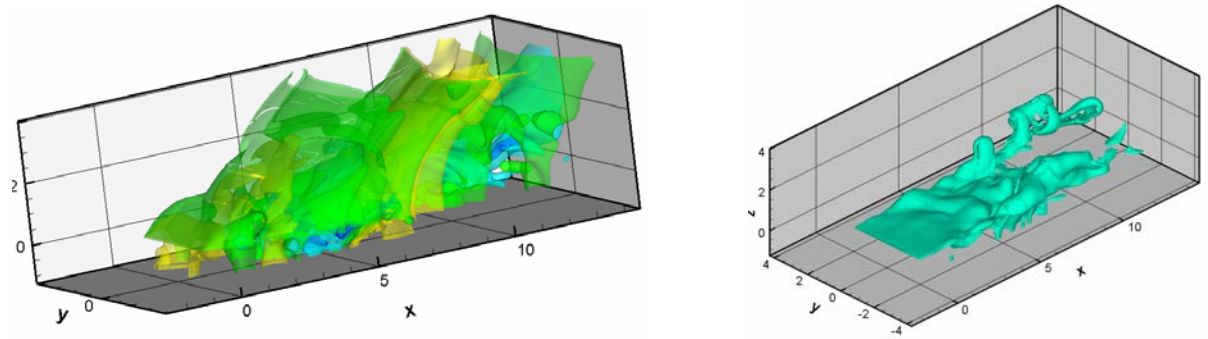

Fig. 4.3: Three-dimensional iso-surfaces of Case (i) cavity flow. (a) Constant pressure and (b) one iso-surface of the magnitude of the vorticity vector. In (b) we observe two vortex tubes in the streamwise direction along the two side edges of the cavity.

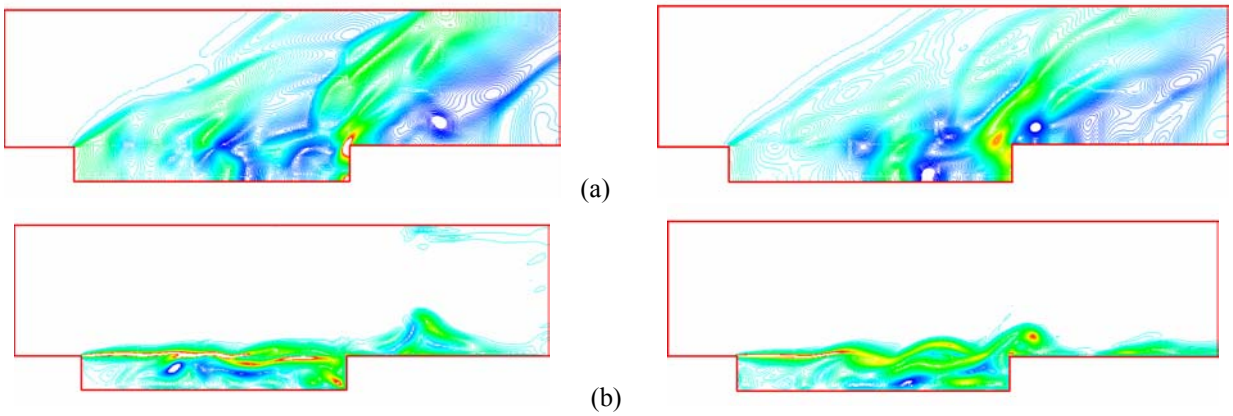

(a)

(b)

Fig. 4.4: Snapshots of on the central plane of the cavity. (a) Pressure and (b) the y-component of vorticity.

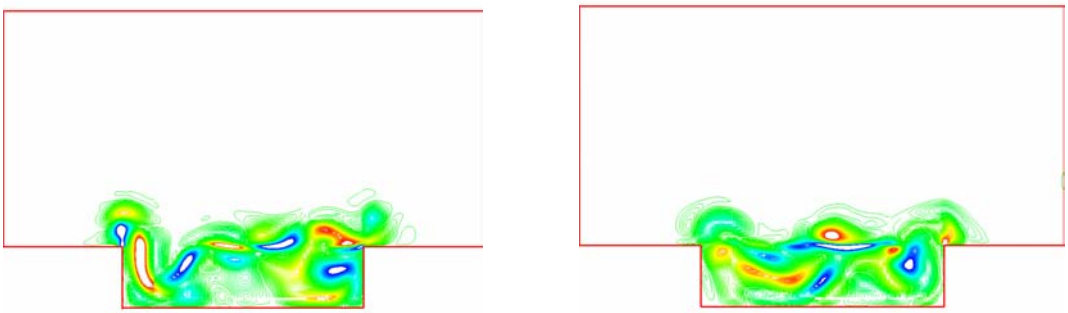

Fig. 4.5: Two snapshots of the x-component of the vorticity vector on a cross section plane at x = 6D from leading edge of the cavity.

Case 2: Mach 2.86 Supersonic Cavity Flows

This case was taken from the experiments conducted by Stalling and Wilcox [20]. The free stream Mach number is M = 2.86. The geometry of the cavity is normalized by the cavity depth and L/D = 12, W/D = 5, where D = 0.5 in. The free stream flow conditions are P_o = 1934 lb/ft2 (or 92600 Pa), and T_o =585 R (or 325 K). The mesh size is about 4.6 million. Since the mesh and the associated domain decomposition are similar to that of Case (i) as shown in Fig. 4.2, no plots about the mesh is provided here.

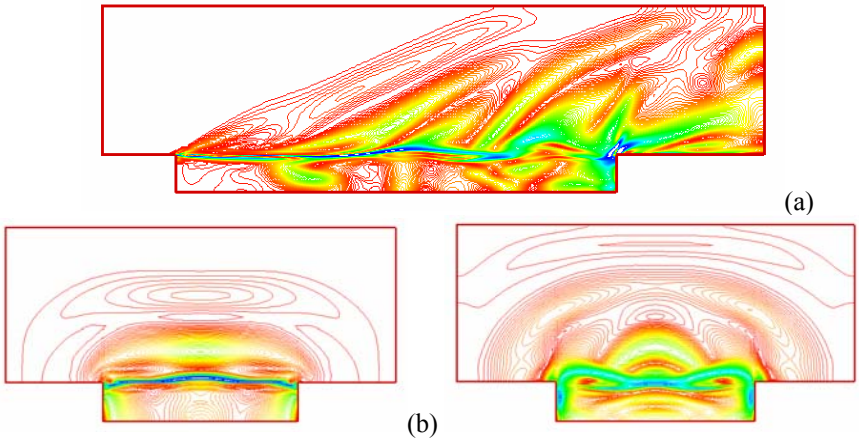

Fig. 4.6: Snapshots of density gradient contours on the cross-sections at (a) y=0, (b) x=6D, and (c) x=9D.

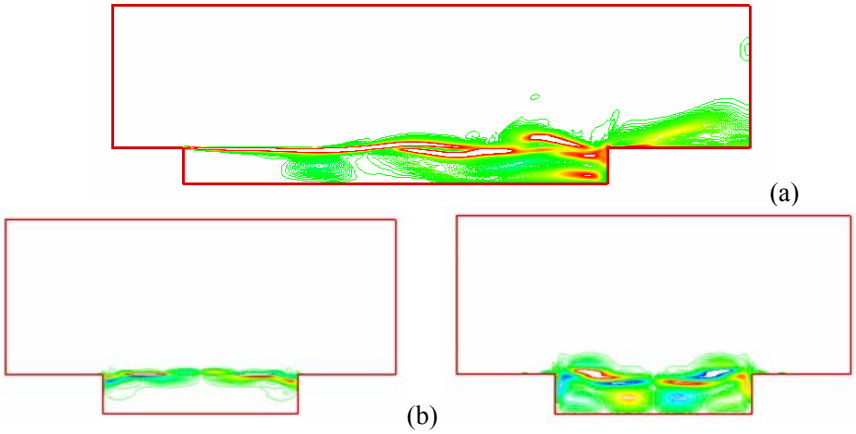

Fig. 4.7: Snapshots of vorticity contour on the cross section planes at (a) y=0, (b) x=6D, and (c) x=9D.

Figure 4.6 shows contours of density gradient magnitudes in the planar view (a) and in the frontal view (b and c). In this case, although the L/D is 12, the shear layer does bend down to touch the bottom of the cavity mainly due to the high Mach number of the free stream. Figure 4.7 shows contours of vorticity magnitudes in the planar view (a)

and in the frontal view (b and c). Although not shown, the flow field is more stable as compared to that of case (i). based on the snapshots in 4.6-7, the flow field is also much more two-dimensional as compared to that of Case (i).

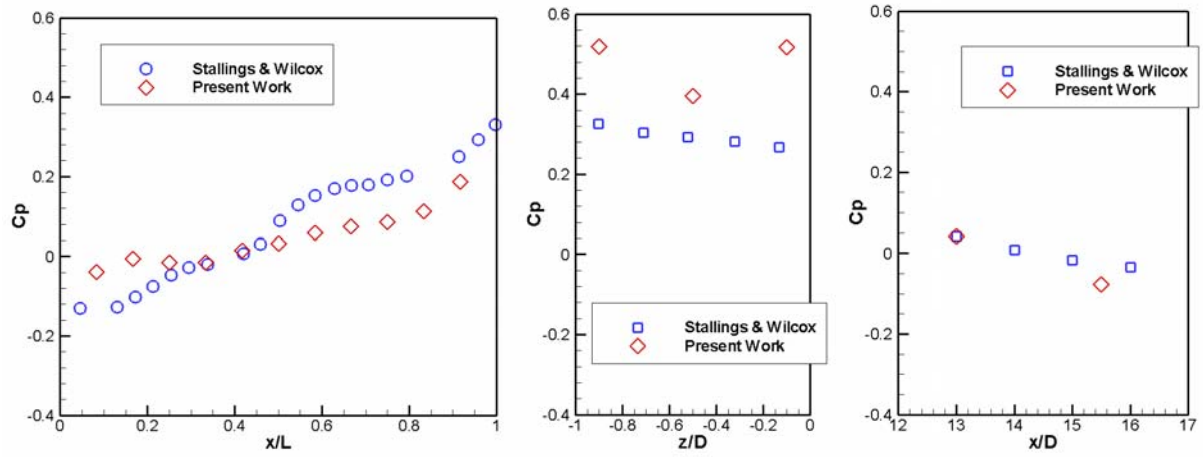

(a) (b) (c)

Fig. 4.8: Time-averaged pressure coefficient Cp distribution. (a) along the centerline on the cavity floor, (b) on the rear wall, and (c) on the plate behind the cavity.

Figure 4.8 shows time-averaged pressure coefficient Cp profile. The pressure coefficient is defined as

$$C_p = \frac{p - p_\infty}{q_\infty}, \tag{4.1}$$

where p_∞ is the free stream static pressure, q_∞ is the free stream dynamic pressure.

Case 3: A Subsonic Cavity Flow

This case was taken from the experiments conducted by Tracy and Plentovich [21]. The free stream Mach number is M = 0.95. The geometry of the cavity is normalized by the cavity depth and L/D = 8, W/D = 4, where D = 2.4 in. The free stream flow conditions are P_o = 12 psi (or 82737 Pa), and T_o =107 F (or 315 K). The mesh size is about 5.4 million. Since the mesh and the associated domain decomposition are similar to that of Case (i) as shown in Fig. 4.2, no plots about the mesh is provided here.

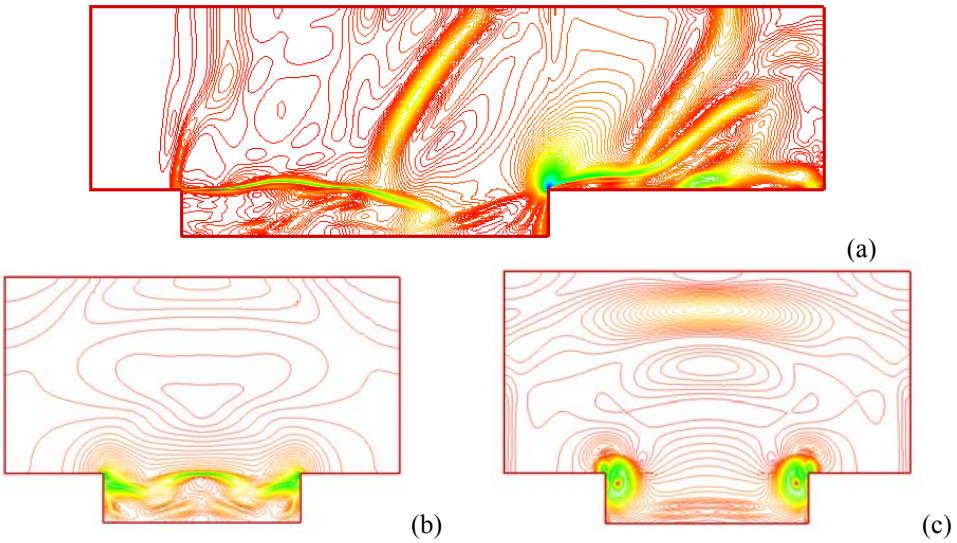

(a)

(b) (c)

Fig. 4.9: Snapshots of density gradient contours on cross section planes at (a) y = 0, (b) x = 4D, and (c) x = 6D.

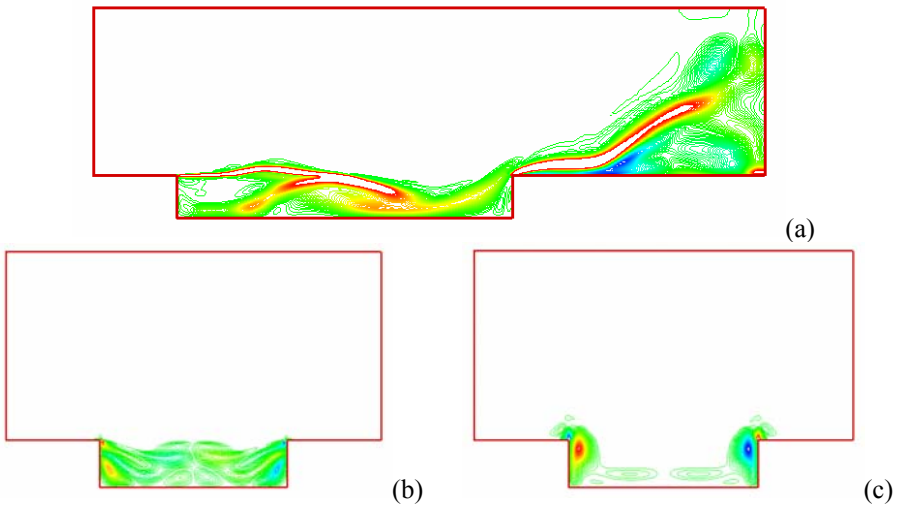

Fig. 4.10: Snapshots of vorticity contours on cross section planes at (a) y = 0, (b) x = 4D, and (c) x = 6D.

Figures 4.9-10 show the snapshots of density gradient and vorticity contours of the three-dimensional flow field on various cross sectional planes. In general, the flow is much more violent due to strong interaction between the free-shear layer and the rearward facing step at the downstream of the cavity. The cavity is "open" owing to tremendous mass exchange between the free stream and the inside of the cavity.

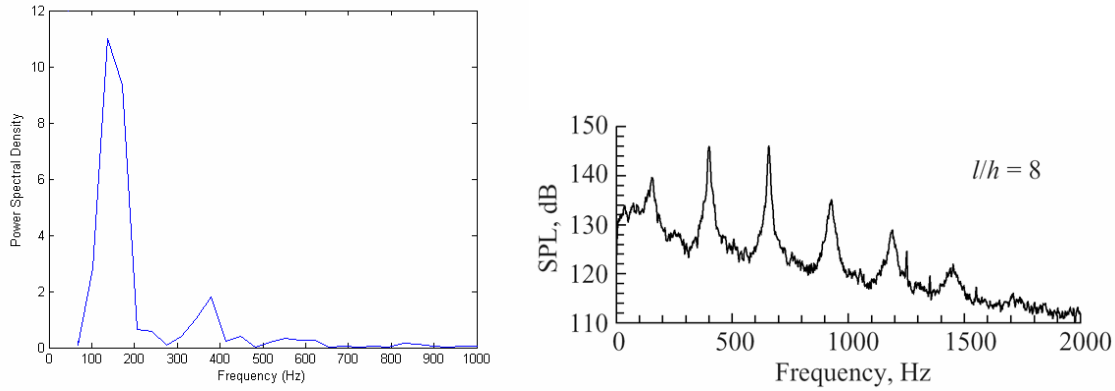

Fig. 4.11: Dominant frequencies of Case (iii). (a) CFD result, and (b) Experimental data [21].

Figure 4.11 shows the calculated dominant frequencies as compared to the experimental results. Shown in the figure, the dominant frequencies are about 140, 400, 660, and 900 Hz. These four frequencies agree well with the first four modes reported by Tracy and Plentovich [21]. For convenience, the SPL-Frequency plot in [21] is also included. In the plot, SPL is defined as

$$SPL = 20\log\left(\frac{p'_{rms}}{2.9\times10^{-9}\ psi}\right), \tag{4.2}$$

where $p'_{\rm rms} = \sqrt{(p')^2}$ is root-mean-square pressure, and p' is the measured unsteady pressure in psi.

V. Conclusion

Preliminary CFD results of three high-speed cavity flows are presented in the present paper. The results were presented qualitative by various snapshots at different cross sectional planes. These figures demonstrate very complex flow features, including traveling acoustic waves, vortex generation at the leading edge, shedding vortices in the free shear layer, and pressure waves impinging on and rebounding from the aft wall. The interactions between the rebounding pressure waves and shed vortices form a feed back loop which leads to self-sustained oscillations. In

all cases, these periodic shear layer deflections in the transverse direction could be clearly discerned. Inward deflection results in mass addition into the cavity; outward deflection expels mass from the cavity. This periodic mass addition/expulsion mechanism enhances fuel/air mixing. Moreover, flapping shock/expansion waves emanating from the upstream bulkhead of the cavity can also enhance fuel/air mixing. Limited code validation has been conducted. In case (ii), the calculated time averaged pressure coefficient profiles have been compared with the experimental data. At the rear bulkhead, numerical result over predicted the magnitude of Cp. CFD results also show smaller recirculation zones around the two corners of the cavity. In the lee of the cavity, CFD results compared well with the experimental measured Cp. In Case (iii), CFD results captured the first four dominant frequencies measured by the experimental works.

References

1. Gruber, M. R., Baurle, R. A., Mathur, T., and Hsu, K.-Y., "Fundamental Studies of Cavity-Based Flame holder Concepts for Supersonic Combustors," Journal of Propulsion and Power, Vol. 17, No. 1, 2001, pp. 146-153
2. Gruber, M. R., Jackson, K., Mathur, T., and Billig, F., "Experiments with a Cavity-Based Fuel Injector for Scramjet Applications," the XIV International Society of Air-Breathing Engines, Florence Italy, September 1999.
3. Ben-Yakar, A., and Hanson, R. K., " Cavity Flame-Holders for Ignition and Flame Stabilization in Scramjets: An Overview," Journal of Propulsion and Power, Vol. 17, No. 4, 2001, pp. 869-877
4. Yu, K. H., Wilson, K. J., and Schadow, K.C., "Effect of Flame-Holding Cavities on Supersonic-Combustion Performance," Journal of Propulsion and Power, Vol. 17, No. 6, 2001, pp. 1287-1295.
5. Baurle, R. A., Tam, C.-J., and Dasgupta, S., "Analysis of Unsteady Cavity Flows for Scramjet Applications," AIAA Paper 2000-3617, Jul. 2000.
6. Tam, C. K. W., and Block, P. J. W., "On the Tones and Pressure Oscillations Induced by Flow over Rectangular Cavities," Journal of Fluid Mechanics, Vol. 89, Part 2, 1978, pp. 373-399.
7. Rockwell, D., and Naudascher, E., "Review – Self-Sustaining Oscillations of Flow Past Cavities," Transaction of ASME, Vol. 100, 1978, pp. 152-165.
8. Rizzetta, D. P., "Numerical Simulation of Supersonic Flow over a Three-Dimensional cavity," AIAA Journal, Vol. 26, No. 7, 1988, pp. 799-807.
9. Vakili, A. D., and Gauthier, C., " Control of Cavity Flow by Upstream Mass-Injection," Journal of Aircraft, Vol. 31, No. 1, 1994, pp. 169-174
10. Sarno, R. L., and Franke, M. E., " Suppression of Flow-Induced Pressure Oscillations in Cavities," Journal of Aircraft, Vol. 31, No. 1, 1994, pp. 90-96
11. Lamp, A. M., and Chokani, N., " Computation of Cavity Flows with Suppression Using Jet Blowing," Journal of Aircraft, Vol. 34, No. 4, 1997, pp. 545-551
12. Anderson, D. A., Tannehill, J. C., and Pletcher, R. H., "Computational Fluid Mechanics and Heat Transfer," McGraw-Hill Book Company, New York, 1984, pp. 189
13. Chang, S.-C., "The Method of Space-Time Conservation Element and Solution Element – A New Approach for Solving the Navier Stokes and Euler Equations," Journal of Computational Physics, Vol. 119, 1995, pp. 295-324.
14. Chang, S.-C., Yu, S.-T., Himansu, A., and Wang, X.-Y., "The Method of Space Space-Time Conservation Element and Solution Element – A New Paradigm for Numerical Solution and Conservation Laws," Computational Fluid Dynamics Review, John Wiley and Sons, UK, 1997.
15. Chang, S.-C., Wang, X.-Y., and Chow, C.-Y, "The Space-Time Conservation Element and Solution Element Method: A New High-Resolution and Genuinely Multidimensional Paradigm for Solving Conservation Laws," Journal of Computational Physics, Vol. 156, 1999, pp. 89-136.
16. Chang, S.-C, Wang, X.-Y., To, W.-M., "Application of the Space-Time Conservation Element and Solution Element Method to One-Dimensional Convection-Diffusion Problem," Journal of Computational Physics, Vol. 165, 2000, pp. 189-215.
17. Zhang, Z. C., Yu, S.-T. J. and Chang, S. C., " A Space-Time Conservation Element and Solution Element Method for Solving the Two- and Three-Dimensional Euler Equations by Quadrilateral and Hexahedral Meshes," Journal of Computational Physics, Vol. 175, No. 1, 2002, pp. 168-199.
18. Chang, S.-C., Himansu, A., Loh, C. Y., Wang, X.-Y., Yu, S.-T., and Jorgenson, P. C. E., " Robust and Simple Non-Reflecting Boundary Conditions for the Space-Time Conservation Element and Solution Element Method," AIAA Paper 99-2077, 1997.

19. Lin, J.-C., and Rockwell, D., " Organized Oscillations of Initially Turbulent Flow past a Cavity," AIAA Journal, Vol. 39, No. 6, 2001, pp.1139-1151
20. Stallings, R. L. Jr., and Wilcox, F. J., "Experimental Cavity Pressure Distributions at Supersonic Speeds," NASA TP-2683, June 1987.
21. Tracy, M.B. and Plentovich, E.B., "Cavity Unsteady-Pressure Measurements at Subsonic and Transonic Speeds," NASA Technical Paper 3669, 1997.